



## Predicting the sensing radius of a coaxial probe based on the probe dimensions

Title	Predicting the sensing radius of a coaxial probe based on the probe dimensions
Author(s)	La Gioia, Alessandra; Santorelli, Adam; O'Halloran, Martin; Porter, Emily
Publication Date	2020-05-19
Publisher	Institute of Electrical and Electronics Engineers
Repository DOI	<a href="https://doi.org/10.1109/TAP.2020.2986708">10.1109/TAP.2020.2986708</a>

**1. What is the problem being addressed by the manuscript and why is it important to the Antennas & Propagation community? (limited to 100 words).**

While the dielectric characterisation of homogeneous biological samples with a coaxial probe is straightforward, there is no consensus on how to associate the dielectric properties acquired from biological heterogeneous samples to the sample tissue content. Generally, a post-measurement histological analysis is conducted on the investigated sample. For an accurate dielectric characterisation, the size of the histology region must correspond to the probe sensing volume, defined by the sensing radius and depth. Since previous studies have examined the dependence of the sensing depth on the probe dimensions and investigated sample, this study is focused on the analysis of the sensing radius.

**2. What is the novelty of your work over the existing work? (limited to 100 words).**

In the literature, the dependence of the sensing radius of a coaxial probe on the probe dimensions in combination with the dielectric properties of the interrogated sample has not been examined yet. Therefore, this study investigates how the sensing radius varies with the probe dimensions, specifically, with the sizes of the inner conductor, insulator, and outer conductor across various tissue-mimicking samples through numerical simulations, previously validated by dielectric measurements. Furthermore, based on the sensing radius values obtained from simulations and measurements, a method for predicting the sensing radius, through use of neural networks, is proposed.

**3. Provide up to three references, published or under review, (journal papers, conference papers, technical reports, etc.) done by the authors/coauthors that are closest to the present work. Upload them as supporting documents if they are under review or not available in the public domain. Enter “N.A.” if it is not applicable.**

- i. La Gioia, M. O’Halloran, A. Elahi, and E. Porter, “Investigation of Histology Radius for Dielectric Characterisation of Heterogeneous Materials,” *IEEE Trans. Dielectr. Insul.*, vol. 25, no. 3, pp. 1065–1080, 2018.
- ii. La Gioia, M. O’Halloran, and E. Porter, “Modelling the Sensing Radius of a Coaxial Probe for Dielectric Characterisation of Biological Tissues,” *IEEE Access*, vol. 6, pp. 46516–46526, 2018.

**4. Provide up to three references (journal papers, conference papers, technical reports, etc.) done by other authors that are most important to the present work. Enter “N.A.” if it is not applicable.**

- i. D. Hagl, D. Popovic, S. C. Hagness, J. H. Booske, and M. Okoniewski, “Sensing volume of open-ended coaxial probes for dielectric characterization of breast tissue at microwave frequencies,” *IEEE Trans. Microw. Theory Tech.*, vol. 51, no. 4, pp. 1194–1206, 2003.
- ii. M. Lazebnik *et al.*, “A large-scale study of the ultrawideband microwave dielectric properties of normal breast tissue obtained from reduction surgeries,” *Phys. Med. Biol.*, vol. 52, no. 10, pp. 2637–2656, 2007.
- iii. P. M. Meaney, A. P. Gregory, J. Seppälä, and T. Lahtinen, “Open-Ended Coaxial Dielectric Probe Effective Penetration Depth Determination,” *IEEE Trans. Microw. Theory Tech.*, vol. 64, no. 3, pp. 915–923, 2016.

# Predicting the Sensing Radius of a Coaxial Probe based on the Probe Dimensions

Alessandra La Gioia, *Student Member, IEEE*, Adam Santorelli, *Member, IEEE*, Martin O'Halloran, *Member, IEEE*, and Emily Porter, *Member, IEEE*

**Abstract**— The coaxial probe technique is used to acquire the dielectric properties of biological tissues in the microwave frequency range. To dielectrically characterise heterogeneous samples, the sensing radius of the probe must be known. Thus, in this study, for the first time, both experimental and numerical investigations were conducted to analyse and model the sensing radius dependence on the probe dimensions. The results suggest that: i) the sensing radius increases linearly with the inner radius of the outer conductor and is not affected by the width of the outer conductor; ii) the inner conductor has higher impact than the insulator on the sensing radius; and iii) although the sensing radius depends on the dielectric properties of the investigated samples, the trend of the sensing radius relative to the probe dimensions is the same across different samples. Furthermore, a method for predicting the sensing radius, through use of neural networks, is proposed.

**Index Terms**— Open-ended coaxial probe, sensing radius, dielectric measurements, EM simulations, neural network.

## I. INTRODUCTION

**D**IELECTRIC PROPERTIES of biological tissues are generally reported in terms of complex permittivity  $\epsilon^*$ , from which relative permittivity  $\epsilon_r$  and conductivity  $\sigma$  are obtained, and are fundamental for the design of microwave (MW) imaging devices [1], [2], and therapeutic technologies, such as MW ablation [3] and hyperthermia systems [4], [5]. Tissue dielectric properties are most commonly acquired using the coaxial probe technique, which is broadband, simple, and non-invasive [6]–[9].

The accuracy of the signal acquired from a coaxial probe depends on the dimensions of the probe with respect to the characteristics of the sample, i.e., the size and distribution of tissue types within the sample [10]–[12]. To this extent, guidelines for selecting the appropriate probe dimensions in relation to the dielectric properties of a sample of infinite size

The research leading to these results has received funding from the European Research Council under the European Union's Horizon 2020 Programme/ ERC Grant Agreement BioElecPro n. 637780. This work was also supported by Science Foundation Ireland (SFI) (grant number 15/ERCS/3276), and the Hardiman Research Scholarship from the National University of Ireland Galway. This work has been developed in the framework of COST Action MiMed (TD1301).

The authors are with the Translational Medical Device Laboratory, National University of Ireland Galway, Ireland, and the University of Texas at Austin, USA (correspondence email: [a.lagioia1@nuigalway.ie](mailto:a.lagioia1@nuigalway.ie)).

were presented in a number of studies [11], [13], [14]. More recent studies have considered the effect of a finite sample size on the accuracy of the dielectric measurement [12], thus analysing the sensing volume of the measurement probe, consisting of sensing depth [15]–[17] and sensing radius [18], [19]. In fact, in case of homogeneous tissue samples of limited size, or homogeneous tissue regions of limited size within heterogeneous samples, knowledge of sensing depth and radius allows defining the minimum longitudinal and radial extent, respectively, within which only the homogeneous tissue of interest is dielectrically interrogated, without the influence of the surrounding materials or tissues [19]. For instance, if the sensing radius (or depth) is larger than the radial extent (or longitudinal extent) of the homogeneous tissue, the acquired dielectric properties do not correspond to the dielectric properties of the tissue of interest, since the properties are affected by other tissues or materials surrounding the tissue of interest. On the other hand, if the sensing radius (or depth) is smaller than the radial extent (or longitudinal extent) of the homogeneous tissue, the dielectric properties of the homogeneous tissue are accurately measured.

In the literature, a number of studies investigated the sensing depth by custom experiments and numerical simulations involving a number of probes with different dimensions [16], [20] and layered materials [21], [22] or biological tissues [17]. Conversely, a limited number of studies have investigated the sensing radius with custom numerical simulations involving a few probe geometries [19], [23] and concentric material samples [12], [24]. For instance, Anderson *et al.* performed simulations with a coaxial probe interacting with a water layer of varying radial extents surrounded by air or metal blocks in the range of 0.2 to 2.0 GHz in order to find the minimum radial extent of water that allowed for accurate dielectric measurements of water [18]. In the study conducted by De Langhe *et al.*, the sensing radius of a coaxial probe was calculated by simulating the interaction of a flanged air-filled coaxial probe with a sample composed of Teflon surrounded by a metal plate [19]. The sample made of Teflon and metal represents the worst case scenario in terms of permittivity contrast, and thus enables the estimation of the maximum radial extent of the sensing volume of the probe. Furthermore, Hoshina *et al.* conducted numerical simulations reproducing the interaction of a flanged large-diameter Teflon-filled coaxial probe with a saline solution at the single frequency of 860 MHz

[23]. Only in the study conducted by Hagl *et al.* the sensing radius was calculated both experimentally and numerically [12]. In particular, Hagl *et al.* analysed the effect of the beaker walls on dielectric acquisitions of reference liquids at different radial distances in the microwave range of 1-20 GHz [12]. Such experimental and numerical design allowed for the calculation of the sensing radius of two probes having different physical dimensions. The outcome of the study by Hagl *et al.* was then used to dielectrically characterise healthy and tumour breast tissue samples in the studies conducted by Lazebnik *et al.* [25], [26]. In fact, in order to accurately characterise highly heterogeneous tissue samples, the estimated sensing radius is generally used to define the radial extent of the sample that undergoes post-measurement histological analysis [17], [25]–[27]. Thus, the values of sensing radius obtained from [12], were used to define the radial extent of the region within the breast samples to analyse histologically in [25], [26].

Thus, knowledge of the sensing radius not only supports the definition of the smallest homogeneous tissue region that can be accurately characterised with a coaxial probe, but also support the dielectric characterisation of highly heterogeneous tissues, which present different tissue types within the sensing radius. As investigation of the sensing radius in the literature has involved only a limited number of probes and samples, in this study, the dependence of the sensing radius on the probe dimensions in combination with the dielectric properties of the interrogated sample is examined. Specifically, we investigate how the sensing radius varies with the dimensions of the probe, specifically, with the sizes of the inner conductor, insulator, and outer conductor across various tissue-mimicking samples.

First, experiments were conducted to estimate the sensing radius of three Keysight probes, which are the most commonly used in the microwave range for characterising biological tissues [28]–[30].

Secondly, after consistency between experiments and simulations was verified, a number of simulations reproducing different combinations of inner conductor, insulator, and outer conductor sizes were performed. For each combination of dimensions, simulations were repeated across four different samples in order to verify that the correlation between the sensing radius and the probe dimensions was consistent across materials having different dielectric properties. Among the simulated samples, breast fat and gland tissue samples were modelled. This sample choice supports breast dielectric characterisation and is crucial for the design of breast MW imaging systems. Simulations were executed across the frequency range of 2–6 GHz, since most MW breast imaging devices operate within this range [1]. The trend of the sensing radius was analysed and modelled across different scenarios with variations in the probe dimensions.

Lastly, simulation results were used to build a linear regression model and a neural network capable of predicting the sensing radius of a coaxial probe based on knowledge of the probe dimensions and the investigated sample properties.

Details about the experimental and numerical design of the study are described in Section II. Both experimental and numerical results are illustrated and discussed in Section III,

and, lastly, the main findings are summarised in the concluding section.

## II. METHODOLOGY

Both dielectric measurements and simulations were conducted on tissue-mimicking samples to calculate the maximum sensing radius of the Keysight slim form, performance, and high temperature probes. Although these probes are designed for homogeneous materials presenting flat surfaces [31], they are the most commonly used probes in recent tissue dielectric studies [30], [32]. Since the three Keysight probes have different dimensions, the results from dielectric experiments involving these probes were processed for an initial analysis of the dependence of the sensing radius on the probe dimensions. Then, the experimental results were validated numerically. Once the consistency between experiments and simulations was verified, for a complete analysis of the sensing radius, a number of probes having different dimensions were modelled numerically and their interactions with a subset of material samples were analysed. The sensing radius was calculated for each simulation scenario. Lastly, the sensing radius data was used to develop a linear regression model and a neural network able to predict the sensing radius of a coaxial probe based on the probe dimensions and the dielectric properties of the interrogated sample.

### A. Maximum sensing radius calculation

As in past studies, the sensing radius is examined through concentric samples consisting of an inner material surrounded by an outer material and is defined as the radial extent of the inner material at which the influence of the outer material is negligible [12]. Specifically, in this study, the sensing radius is defined as the width of the inner material at which the outer material ceases to contribute to the acquired dielectric properties, within the uncertainty of the measurement system (i.e., the distance at which only the relative permittivity of the inner material is detectable, within the uncertainty of the measurement).

By considering the EM signal propagating across the inner and outer materials, the sensing radius value at a certain frequency is related, in turn, to the impedance mismatch between the probe and the inner material, the signal attenuation across the inner material, and the impedance mismatch between the inner and outer materials. Thus, the calculation of the sensing radius can be formulated in terms of electric field sensed by the probe (i.e., field reflected from the sample consisting of an inner material surrounded by a concentric outer material) as follows:

$$\left(1 - \frac{Z_1 - Z_0}{Z_1 + Z_0}\right)^2 \frac{Z_2 - Z_1}{Z_2 + Z_1} e^{2\gamma_1 r_1} \leq u_E \quad (1)$$

where  $Z_0$ ,  $Z_1$  and  $Z_2$  are the characteristic impedances of the coaxial probe, inner material and outer material, respectively,  $r_1$  is the radius of the inner material,  $\gamma_1$  is the propagation constant across the inner material, and  $u_E$  refers to the uncertainty of the acquired electric field with reference to the incident electric field. In (1),  $\frac{Z_1 - Z_0}{Z_1 + Z_0}$  and  $\frac{Z_2 - Z_1}{Z_2 + Z_1}$  are the reflection coefficients from

the inner and outer materials, respectively, which are related to both the characteristics of the probe (i.e., dimensions and dielectric constant of the insulator) and the dielectric properties of the materials. Furthermore, the term  $\left(1 - \frac{Z_1 - Z_0}{Z_1 + Z_0}\right)^2$  refers to the forward and backward components of the electric field transmitted across the inner material obtained by considering the reflection due to the impedance mismatch between the probe and the inner material  $\left(\frac{Z_1 - Z_0}{Z_1 + Z_0}\right)$ , the term  $\frac{Z_2 - Z_1}{Z_2 + Z_1}$  refers to the electric field reflected from the second material (due to the impedance mismatch between the inner and outer materials), the term  $e^{2\gamma_1 r_1}$  refers to the field attenuation across the inner material by considering both forward and backward signals. Thus, (1) allows for the estimation of the inner material radius  $r_1$  at which the electric field sensed by the probe is considerably lower than the incident electric field, i.e., lower than  $u_E$ . This method of assessing the sensing radius assumes that the EM signal propagates in Transverse Electro-Magnetic (TEM) mode across the two concentric materials, that there is no reflection due to fringing field, and that the sensing volume is a perfect hemisphere with radial extent equivalent to the longitudinal extent. Due to the inapplicability of the assumptions in (1) in experimental scenarios, in this study, the sensing radius has been calculated both experimentally and numerically as reported in [24].

Furthermore, in this work, the maximum sensing radius refers to the maximum value that the sensing radius of a given coaxial probe can assume, since the sensing radius varies based on the dielectric properties of tissues constituting the investigated sample [27].

#### A.1. Measurement methodology

Dielectric measurements were performed using each of the three Keysight probes connected to the Agilent E5063A network analyser by following the protocol previously performed with the Keysight slim form probe in [27]. The Keysight slim form, performance and high temperature probes have different dimensions of inner conductor, insulator, and outer conductor. The probe dimensions, which are illustrated in Fig. 1, are reported in Table I for each of the Keysight probes. Since the probe datasheet reports only information regarding the size of the outer conductor, the other probe dimensions were measured with a calliper through reverse engineering.

TABLE I  
DIMENSIONS OF THE THREE KEYSIGHT PROBES.  $a$ ,  $b$ ,  $c$  AND  $r$  REFER TO PROBE FEATURES ILLUSTRATED IN FIG. 1.

Keysight probes	$a$ [mm]	$c$ [mm]	$b$ [mm]	$r$ [mm]
<i>Slim form</i>	0.25	0.50	0.75	1.10
<i>Performance</i>	0.30	0.50	0.80	4.75
<i>High temperature</i>	0.35	1.00	1.35	9.50

The measurement sample used to calculate the maximum sensing radius in this study was manufactured as described in [27]. Composed of Teflon and saline solution, this sample allows for the estimation of the maximum sensing radius based on the fact that these materials represent the scenario with the highest contrast in complex permittivity that can be found

across biological tissues [27]. Thus, the sensing radius for measurements of biological tissues is expected to be smaller than the maximum sensing radius.

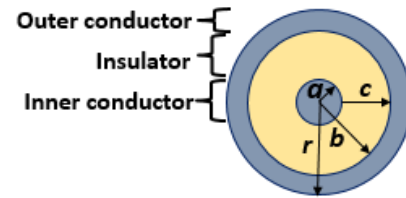


Fig. 1. Dimensions of the coaxial probe:  $a$  is the radius of the inner conductor,  $c$  is the insulator width,  $b$  (obtained by summing  $a$  and  $c$ ) is the inner radius of the outer conductor, and  $r$  is the total radius of the probe.

The sample was obtained by drilling circular apertures of different radii into a Teflon block and immersing the drilled block in 0.1 M NaCl solution (saline). Both the thickness of the Teflon block and the size of the Teflon apertures were chosen based on the results of preliminary experiments [27]. Furthermore, the increase in size of the Teflon apertures was chosen based on the resolution of the drilling machine. The thickness of the Teflon block was selected so that it was larger than the sensing depth of the probe. The radius of the Teflon aperture was chosen by ensuring that the sensing radius of each probe was within the smallest and the largest aperture. Specifically, the Teflon block has a thickness of 10 mm and its apertures have radii of: 0.5 mm, 1 mm, 1.25 mm, 1.75 mm, 2.5 mm, 3 mm, 4 mm, and 5 mm, respectively. Dielectric measurements were performed with each of the three probes across all Teflon apertures immersed in 0.1 M NaCl solution. An example of the dielectric measurement performed on a Teflon aperture with the performance probe is provided in Fig. 2.

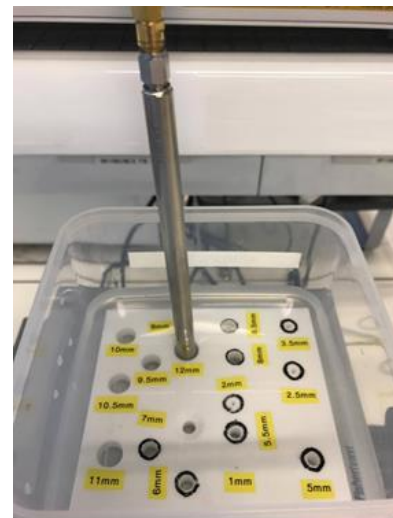


Fig. 2. Keysight performance probe in contact with the Teflon block immersed in 0.1 M NaCl solution. On the Teflon block, the sizes of the apertures are labelled and, for apertures smaller than the total radius of the probe, the size of the probe is marked in black around the apertures in order to facilitate probe positioning.

Before each set of measurements, the system was calibrated using the three-load standard procedure and the quality of the calibration was verified by measuring the dielectric properties of 0.1 M NaCl, a standard reference liquid [33]. Before and after

each calibration, the temperature of the calibration and validation liquids were recorded. Recordings of 0.1 M NaCl were compared to the known model properties, confirming that the measurement uncertainty was consistently below 2.5%. For each measurement, the relative permittivity and conductivity were acquired at 21 frequency points on a linear scale over the frequency range of 2–6 GHz.

For each measurement, the sample was brought to the probe tip using a lift table. A stable contact between the probe and the sample was ensured by visual inspection. The temperature of the immersion solution (0.1 M NaCl) surrounding the Teflon block was also recorded. For apertures smaller than the size of the probe, the measurement was more difficult to perform due to difficulty in visualising the presence of air bubbles at the probe tip, and the position of the probe with respect of the Teflon walls. Therefore, in order to ensure that the probe location was concentric to the Teflon aperture (i.e., that the Teflon aperture was centred with respect to the probe), the probe size was marked around the smaller apertures, as illustrated in Fig. 2. Furthermore, for each probe, measurements were repeated after three different calibrations to confirm the measurement outcome.

For each probe and each calibration, the maximum sensing radius was obtained by comparing single frequency measurements, or measurements averaged across frequency range, acquired across all apertures. Then, the maximum sensing radius was estimated as the radius of the Teflon aperture at which, the measured relative permittivity was equal to the relative permittivity of saline, within the uncertainty of the system (2.5%).

Measurements results were validated with numerical simulations reproducing the experimental scenarios. Details on the simulation models are reported in the following subsection.

### A.2. Numerical methodology

The three Keysight probes were modelled numerically. The geometry of the probes was designed with the features reported in Table I. For all probes, nickel was assigned as the material for the inner and outer conductors, and Teflon was assigned as the material for the insulator. Since information regarding the materials of the probes are not reported in the probe datasheet, different combinations of materials were tested for numerical simulations in previous studies [27]. Nickel and Teflon were selected, since these materials ensure the best match between simulated and measured dielectric properties.

The dielectrically interrogated samples were modelled to reproduce the measurement samples consisting of 0.1 M NaCl solution surrounded by Teflon. As with the experiments, cylindrical samples with different radii of saline solution surrounded by Teflon were created; however, more samples with intermediate values of radius were included as they could be easily numerically modelled. Thus, the saline solution was modelled with variable radius ranging from 0.5 to 5 mm with 0.25 mm discrete steps, surrounded by Teflon having radius much larger than that of saline. Once the geometry of the samples was created, the dielectric properties of saline and Teflon were assigned to the simulation model. Specifically, one

pole Cole–Cole models were fitted to the dielectric data measured experimentally from the 0.1 M NaCl solution and Teflon using the two-stage genetic algorithm [34]. The parameters of the Cole–Cole model for saline and Teflon are summarised in Table II.

TABLE II  
ONE POLE COLE-COLE PARAMETERS FOR CONCENTRIC SIMULATED  
SAMPLES CONSISTING OF SALINE AND TEFLON

Parameters	Saline	Teflon
$\epsilon_{\infty}$	5.1700	1.4600
$\sigma_s$ (S/m)	0.9600	0.0030
$\Delta\epsilon$	72.9300	1.0000
$\tau$ (s)	8.78e-12	1e-12
$\alpha$	0.0071	0.0010

Once the design of the numerical models was completed, simulations were executed in COMSOL Multiphysics version 5.3. Simulation settings are reported in [27]. After the simulations were solved, the EM field across the sample materials in proximity of the probe tip and the  $S_{11}$  parameters (i.e., reflection coefficient), from the probe–sample interface were analysed.  $S_{11}$  parameters were converted into complex permittivity values using the open-ended coaxial probe antenna model [35]. The relative permittivity and conductivity data obtained from each set of simulations were analysed to calculate the sensing radius for each of the three Keysight probes. As with the experimental data, the sensing radius was quantified as the radius at which only the relative permittivity of the saline solution is detectable within 2.5% (i.e., the measurement uncertainty). An illustrated example of calculating the sensing radius from numerical data is reported in [24].

The same numerical procedure was followed for the calculation of the sensing radius across different probe designs and samples. Details about the geometry of the modelled probes and the interrogated samples are reported in the following subsection.

### B. Sensing radius calculation across different probe designs and samples

In order to expand the investigation of sensing radius beyond the fixed dimensions of the Keysight probes, a number of other probes with different geometries were modelled. Specifically, the dimensions of the inner conductor and insulator were varied, by either maintaining or increasing the dimension of the inner radius of the outer conductor. Since preliminary simulations demonstrated that the width of the outer conductor does not impact the sensing radius, an outer conductor having a fixed width of 1 mm was used for all probe geometries. As a demonstration that the width of the outer conductor does not impact the sensing radius, Fig. 3 illustrates the electric field decay across the half cross-section of the interrogated sample (saline surrounded by Teflon in this case) with the two probes having the same inner conductor radius of 0.25 mm and the same insulator width of 0.5 mm but different outer conductor widths of 0.5 mm and 2 mm, respectively. Specifically, Fig. 3 depicts a simplified 2D axis-symmetric geometry, with the radial and axial distances shown in mm horizontally and

vertically, respectively. In Fig. 3, the electric field isolines at 4 GHz are marked, with the last isoline referring to the location where the electric field decay is 40 dB. Although the two probes in Fig. 3 have different outer conductor widths, the electric field isolines at 4 GHz (as with any other frequency) have the same radial and longitudinal extents, thus highlighting that the extent of electric field decay is the same for the two probes.

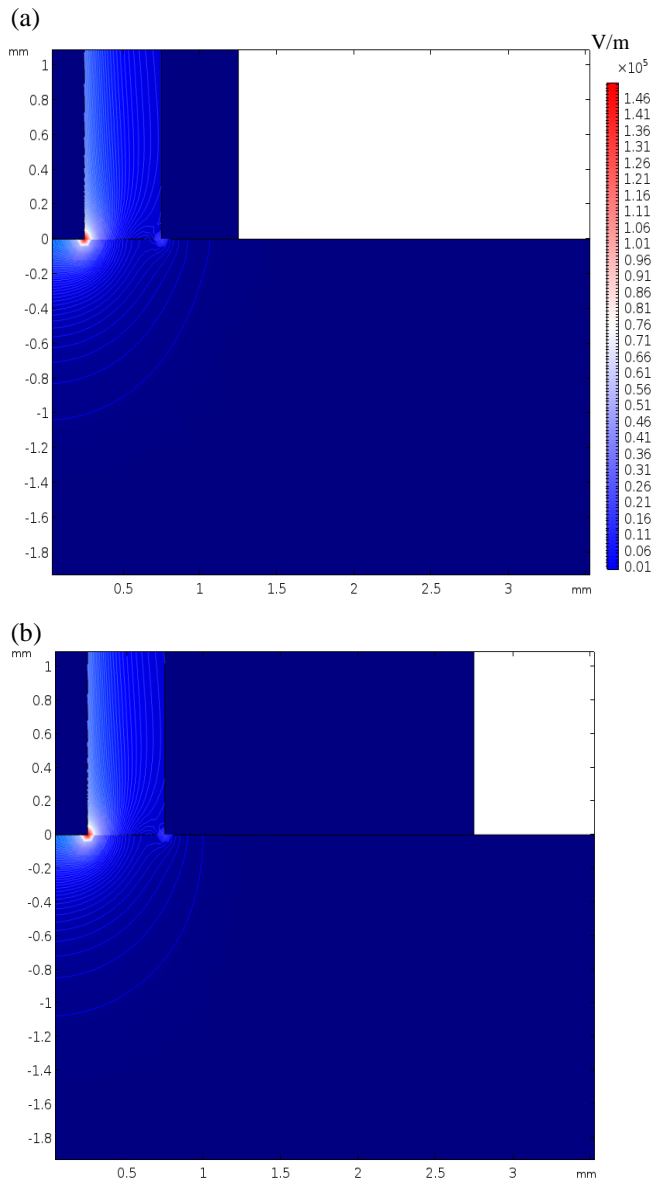


Fig. 3. Contour plot of the electric field magnitude (V/m) at 4 GHz of two simulated probes having the same inner conductor radius of 0.25 mm, the same insulator width of 0.5 mm, but different outer conductor widths of 0.5 mm and 2 mm, respectively.

For the probe geometry, the slim form probe defined the minimum probe size, and the maximum probe size was selected by considering the coaxial line cut-off frequency. In total, 12 probes were modelled with different dimensions and assigned to four categories (or subsets of probe dimension combinations), as listed in Table III. Each combination subset consists of four probes having different size. The subsets S1, S2 and S4 have the slim form probe CP1 as the initial probe size. For the first category (S1), the insulator width  $c$  was kept fixed, and the radius of the inner conductor  $a$  was gradually increased

by 0.25 mm; thus also the inner radius of the outer conductor  $b$  gradually increased by 0.25 mm. For the second category (S2),  $a$  was kept fixed, and  $c$  was gradually increased by 0.5 mm; thus also  $b$  gradually increased by 0.5 mm. For the third category (S3),  $b$  was kept fixed, and  $a$  was gradually increased by 0.25 mm while  $c$  was gradually decreased by 0.25 mm. Lastly, for the fourth category (S4),  $a$  was gradually increased by 0.25 mm while  $c$  was gradually increased by 0.5 mm; thus  $b$  gradually increased by 0.75 mm.

TABLE III  
LIST OF PROBE DIMENSION COMBINATIONS (CP1,...,CP12)  
GROUPED IN FOUR CATEGORIES (S1,...,S4).  $a$ ,  $b$  AND  $c$  REFER TO  
PROBE FEATURES IN FIG.1.

Category	Coaxial probes	$a$ [mm]	$c$ [mm]	$b$ [mm]
S1	CP1	0.25	0.50	0.75
	CP2	0.50	0.50	1.00
	CP3	0.75	0.50	1.25
	CP4	1.00	0.50	1.50
S2	CP1	0.25	0.50	0.75
	CP5	0.25	1.00	1.25
	CP6	0.25	1.50	1.75
	CP7	0.25	2.00	2.25
S3	CP8	0.25	1.25	1.50
	CP9	0.50	1.00	1.50
	CP10	0.75	0.75	1.50
	CP4	1.00	0.50	1.50
S4	CP1	0.25	0.50	0.75
	CP9	0.50	1.00	1.50
	CP11	0.75	1.50	2.25
	CP12	1.00	2.00	3.00

The slim form probe CP1 is included across three categories, for ease in analysis. Similarly, the probes CP4 and CP9 are included also in categories S3 and S4, respectively. Among the probes listed in Table III, the performance probe is not included due to its dimensions  $a$ ,  $b$  and  $c$  that are very close to the slim form probe CP1 (the slim form probe and the performance probe have different total radius because of the width of the outer conductor that does not affect the sensing radius). The high temperature probe is not included either, since its dimensions are very close to the probe CP5.

For each probe geometry, simulations across different concentric samples were conducted in order to verify that the correlation between the sensing radius and the probe geometry was consistent across materials having different dielectric properties. Concentric samples modelled as described in Section II.A.2 were simulated with the four material combinations detailed in Table IV. The sample having saline as inner material and Teflon as outer material was selected, as specified in Section II.A, since it enables calculation of the maximum sensing radius. The locations of the two materials

were then swapped to model another sample. The dielectric properties assigned to Teflon and saline are reported in Table II. Furthermore, two samples consisting of breast gland and fat tissues were modelled to support breast tissue dielectric characterisation, which is fundamental for MW breast imaging systems. The dielectric properties of breast tissue assigned to the modelled samples were from the IT'IS database [36].

TABLE IV

MODELLED CONCENTRIC MATERIALS/TISSUES WITH THEIR RATIO IN RELATIVE PERMITTIVITY. THE AVERAGE RELATIVE PERMITTIVITY VALUES OF THE MATERIALS/TISSUES ACROSS THE RANGE 2–6 GHz ARE SPECIFIED IN BRACKETS.

Samples	Inner material	Outer material	Ratio in $\epsilon_r$
Saline In–Teflon Out	Saline ( $\epsilon_r=74.00$ )	Teflon ( $\epsilon_r=2.15$ )	34:1
Teflon In–Saline Out	Teflon ( $\epsilon_r=2.15$ )	Saline ( $\epsilon_r=74.00$ )	1:34
Gland In–Fat Out	Gland ( $\epsilon_r=53.50$ )	Fat ( $\epsilon_r=4.80$ )	10:1
Fat In–Gland Out	Fat ( $\epsilon_r=4.80$ )	Gland ( $\epsilon_r=53.50$ )	1:10

For each of the 48 simulation scenarios (12 probe geometries x 4 concentric samples), besides the calculation of the sensing radius from the  $S_{11}$  parameters converted into permittivity, as detailed in Section II.A, the electric field decay around the probe was analysed in order to find a correlation between the sensing radius and the dissipated EM signal. Also, for each scenario, the sensing radius (calculated for 21 simulation frequencies) was averaged across the frequency range, and it was verified that the average sensing radius was within 5% from the sensing radius estimated for the central simulation frequency (4 GHz), as previously observed in [24].

For each probe dimension combination subset, and for each concentric sample, the estimated average sensing radius values were represented with first or second degree polynomial curves (fitting the average sensing radius data). The parameters of the functions fitting the numerical sensing radius data are reported in Section III.B according to (2) and (3):

$$f(x) = p_3 x^2 + p_2 x + p_1, \quad (2)$$

$$f(x) = p_2 x + p_1, \quad (3)$$

where  $x$  is one of the probe dimensions,  $f(x)$  is the sensing radius,  $p_1$  is the intercept,  $p_2$  is the first degree coefficient and  $p_3$  is the second degree coefficient.

Then, the numerical sensing radius data was further processed to develop a linear regression model and build a neural network, details of which are reported in the next subsection.

### C. Sensing radius prediction

Machine learning techniques enable data prediction from *a priori* information after creating a generalisation of the input–output relationship derived from a set of training data.

In this study, a linear regression model and a neural network were developed from the simulation dataset of 48 observations detailed in Section II.B. Each observation consists of four input features and one output target. The four inputs of the two models are: the radius of the inner conductor,  $a$ , the inner radius of the outer conductor,  $b$ , and the average relative permittivity of the two materials constituting the concentric sample,  $\epsilon_{r1}$  and

$\epsilon_{r2}$ . The insulator width  $c$  was not used as input parameter since it is not an independent parameter; in fact,  $c$  is the mathematical difference between  $b$  and  $a$ . The output target for each observation is the sensing radius calculated from the simulations described in Section II.B.

Both models were trained with 90% of the data, and then tested with the remaining 10%.

Specifically, for the regression model, the training dataset was used to obtain a regression line that relates the sensing radius to the probe dimensions and relative permittivity values of the two concentric tissues, as follows:

$$y = p_1 + p_2 a + p_3 b + p_4 \epsilon_{r1} + p_5 \epsilon_{r2}, \quad (4)$$

where  $y$  is the sensing radius,  $a$  and  $b$  are the dimensions of the probe illustrated in Fig. 1,  $\epsilon_{r1}$  and  $\epsilon_{r2}$  are the average relative permittivities of the inner and outer tissues, respectively,  $p_1$  is the intercept, and  $p_2, p_3, p_4$  and  $p_5$  are the coefficients obtained from the data fitting. The resulting regression model was then tested with the remaining data.

On the other hand, the neural network was constructed with 2 hidden layers, the first layer consisting of 5 neurons and the second layer consisting of 2 neurons. The network was trained and tested (with the same datasets used for the linear regression) across ten iterations using the Levenberg–Marquardt algorithm. Each iteration produced one trained network, and, among the 10 resulting nets, the network providing the lowest mean squared error (MSE) in the testing stage was selected as the final trained network.

The performance of the two models was then evaluated by comparing the predicted sensing radius values with the output targets from the testing datasets.

Lastly, the models were further tested by predicting the sensing radius of the performance and high temperature probes for the sample having saline as inner material and Teflon as outer material, since the data obtained from experiments and simulations using these two Keysight probes were not included in the original 48 simulation scenarios used to develop and test the models.

Details regarding the performance of the linear regression model and the neural network are reported in Section III.C.

## III. RESULTS AND DISCUSSION

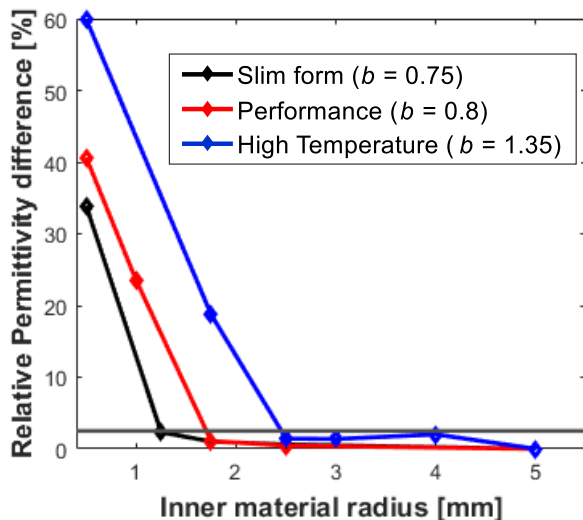
In the first subsection, both experimental and numerical results aimed at calculating the maximum sensing radius of the Keysight probes are reported. In the second subsection, the dependence of the sensing radius on the probe dimensions is examined by modelling the numerical results. Then, in the third subsection, the performance of the linear regression model and the neural network developed with the numerical data is detailed. Lastly, the main findings of this study are summarised and discussed.

### A. Maximum sensing radius calculation

In Fig. 4, both experimental and numerical data from the three Keysight probes is illustrated for the calculation of the maximum sensing radius. In the measurement plot (Fig. 4 a), the percent difference between the relative permittivity acquired from each Teflon aperture and the relative permittivity

of the 0.1 M NaCl solution is plotted as a function of the radius of the Teflon aperture. In the same way, in the simulation plot (Fig. 4 b), the percent difference between the relative permittivity acquired from each of the different sized concentric samples (consisting of saline as inner material and Teflon as outer material) and the relative permittivity of the saline solution is plotted as a function of the radius of the inner material (saline). Both measurement and simulation plots refer to acquired data averaged across frequency. Also, in both plots, the value of the measurement uncertainty (2.5%) is indicated with a horizontal line to graphically facilitate the estimation of the sensing radius. In particular, for each trace (black trace referring to the slim form probe, red trace to the performance probe, and blue trace to the high temperature probe), the sensing radius corresponds to the radius at which the percent difference is approximately 2.5%. Specifically, in Fig. 4 b, the sensing radius values are marked where the relative permittivity difference lines intercept the horizontal threshold trace.

(a)



(b)

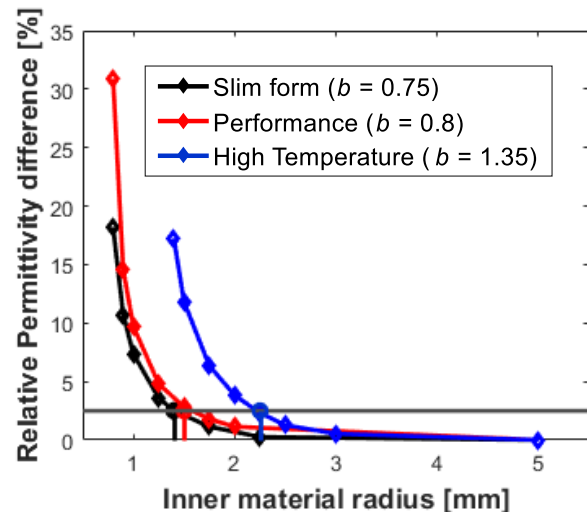


Fig. 4. Determination of the maximum sensing radius for the three Keysight probes through (a) measurements and (b) simulations.

From the measurement plot in Fig. 4 a, it can be observed that the sensing radius estimated for the slim form, performance, and high temperature probes is approximately 1.25 mm, 1.7 mm

and 2.5 mm, respectively. From the simulation results in Fig. 4 b, the sensing radius was found to be 1.4 mm, 1.5 mm and 2.25 mm for slim form probe, performance probe, and high temperature probe, respectively. The differences in values between the measurement and simulation are attributed to the increased number of Teflon apertures that were numerically modelled. Therefore, a higher resolution in the transition of dielectric properties relative to changes in radii is achieved in simulation. For this reason, the three curves in Fig. 4 b show an exponential trend. Such exponential trend is not detected in Fig. 4 a due to the limited changes in the radius of the inner material (because of the resolution of the drilling machine). Furthermore, differences in values between the measurement and simulation can be attributed to measurement confounders, such as the presence of microscopic air bubbles at the probe tip or unstable contact between the probe and the Teflon. However, since the difference between the measured and simulated sensing radius data is always within 0.25 mm, the simulations are in good agreement with the measurements.

These initial results showed that the sensing radius increases with the size of the probe, since the three Keysight probes have increasing size. In fact, as reported in Table I, the inner radius of the outer conductor of the slim form probe, performance probe and high temperature probe is 0.75 mm, 0.8 mm, and 1.35 mm, respectively. The dependence of the sensing radius on the probe size is better examined through numerical results in the following subsection.

### B. Sensing radius analysis and modelling

In this subsection, the average sensing radius data obtained from the numerical simulations are plotted, in turn, for each subset of probe dimension combinations (reported in Table III).

In order to examine the trend of the sensing radius for the subset S1, in Fig. 5, the average sensing radii calculated for the four probes (CP1, CP2, CP3 and CP4) are plotted versus the increasing radii of the inner conductor.

From the plot in Fig. 5, it is clear that the sensing radius (which single values are indicated with stars) increases linearly with the inner conductor radius. The linear trend is highlighted by fitting regression lines to the data points. The coefficients,  $R^2$  values and root mean squared errors (RMSE) of the regression lines are reported in Table V for each of the four simulated samples. The  $R^2$  and RMSE values listed in the table confirm the quality of the fitting.

Although the trend is linear across all simulated samples, the sensing radius values vary according to the materials constituting the samples, as demonstrated in [24]. In fact, from Fig. 5, we can observe that the smallest values of sensing radius are obtained for the sample having breast fat as inner tissue and breast gland as outer tissue. On the other hand, the largest values of sensing radius are obtained for the sample having saline as inner material and Teflon as outer material, thus confirming that, in this case, the estimated sensing radius is equivalent to the maximum sensing radius.

For a specific probe geometry, the sensing radius trend across samples observed in Fig. 5 is consistent with the numerical and experimental findings in [24], where the dependence of the sensing radius on the dielectric properties of the interrogated materials was examined. Specifically, in [24], it was observed that the sensing radius is greatly affected by the relative

permittivity of the material in contact with the inner conductor of the probe. Furthermore, in [24] it was found that the sensing radius increases with the contrast in relative permittivity between two concentric materials. In fact, between two samples consisting of the same materials but with swapped locations, the sensing radius is higher for the sample having an inner material with higher relative permittivity than the outer material. For instance, between the two Teflon and saline samples, the sensing radius is higher for the sample with saline as inner material than it is for the sample with Teflon as inner material. Lower values of sensing radius for samples having an inner material with lower relative permittivity can be due to the impedance mismatch between the probe and the inner material, which tends to be higher for lower permittivity materials. Furthermore, the sensing radius values for the two samples having higher contrast in relative permittivity, the Teflon and saline samples, are higher than for the breast samples, which have lower contrast in relative permittivity, as illustrated in Table IV.

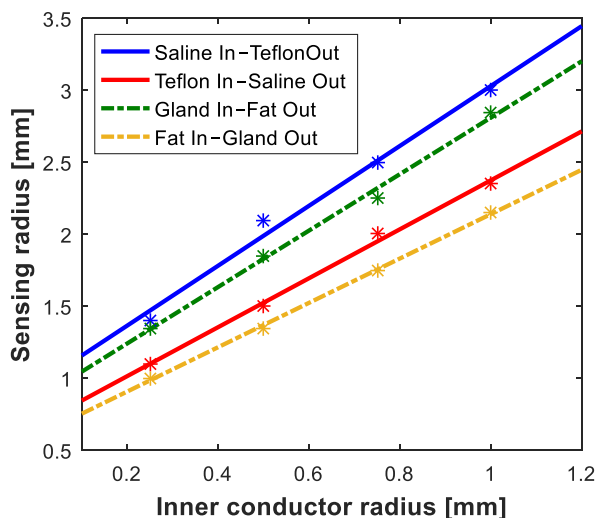


Fig. 5. Regression lines (which parameters are presented in Table V) fitting the sensing radius dependence on the inner conductor radius for the scenario S1, where only  $a$  and then  $b$  are increased.

Samples	$p_2$	$p_1$	$R^2$	RMSE
Saline In-Teflon Out	2.08	0.95	0.987	0.0949
Teflon In-Saline Out	1.70	0.68	0.996	0.0433
Gland In-Fat Out	1.96	0.85	0.994	0.0592
Fat In-Gland Out	1.54	0.60	0.999	0.0194

The same trend of the sensing radius varying with the sample composition is observed across all other scenarios of different probe dimension combinations.

Next, in Fig. 6, the average sensing radii calculated across the scenarios S2 are plotted versus the widths of the insulator. The four probes of the subset S2 have increasing insulator widths but same inner conductor radius. The data in Fig. 6 illustrates the linear relationship between the sensing radius and the insulator width across all samples. Thus, the data was

interpolated with regression lines, the parameters of which are listed in Table VI for each simulated sample. The lines in Fig.5 have varying gradient and are not parallel.

In Fig. 7, the data from subset S3 is illustrated. Specifically, the average sensing radii calculated across probes having fixed inner radius of the outer conductor are plotted versus the increasing radii of the inner conductor. In this case, the trends were not found to be linear. Thus, the data was interpolated with second degree polynomials, with coefficients and RMSE values summarised in Table VII. The fitting curves illustrate that the sensing radius is greatly dependent on the radius of the inner conductor. For the subset S3, since the insulator width decreases while the inner conductor radius increases, while the relationship between the sensing radius and the inner conductor radius is directly proportional, the relationship between the sensing radius and the insulator width is inversely proportional.

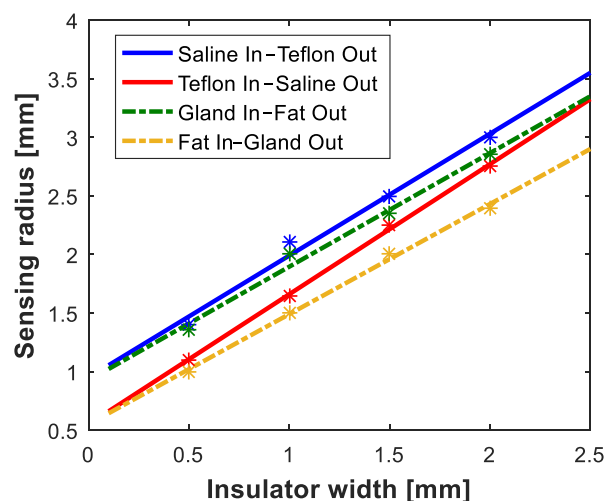


Fig. 6. Regression lines (which parameters are in Table VI) fitting the sensing radius dependence on the insulator width for the scenario S2, where only  $c$  and then  $b$  are increased.

TABLE VI  
PARAMETERS,  $R^2$  VALUE AND RMSE OF THE REGRESSION LINES IN FIG.6.

Samples	$p_2$	$p_1$	$R^2$	RMSE
Saline In-Teflon Out	1.04	0.95	0.987	0.0949
Teflon In-Saline Out	1.11	0.55	0.999	0.0296
Gland In-Fat Out	0.97	0.93	0.987	0.0887
Fat In-Gland Out	0.94	0.55	0.997	0.0387

Furthermore, the curves of Fig. 7 follow different exponential trends across samples. However, the sensing radius increases faster for samples with higher contrast in relative permittivity and/or inner materials with higher dielectric properties than for samples with lower contrast in relative permittivity and/or inner materials with lower dielectric properties.

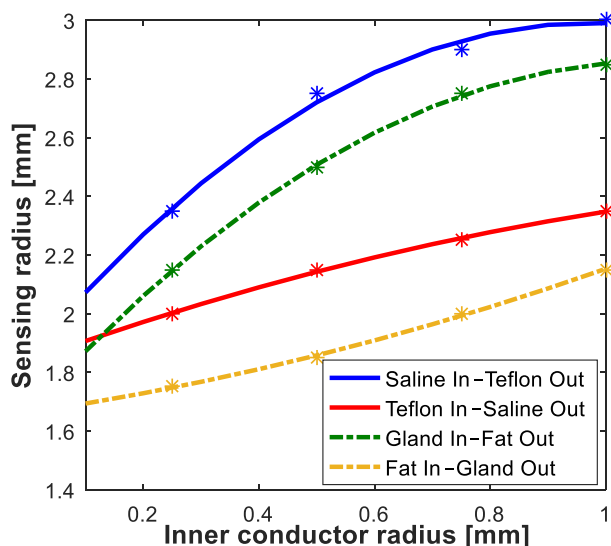


Fig. 7. Sensing radius vs inner conductor radius for the scenario S3, where  $b$  is kept constant while  $a$  increases and  $c$  decreases. The data is interpolated with second degree polynomials, with parameters reported in Table VII

TABLE VII  
PARAMETERS, AND RMSE OF THE SECOND DEGREE POLYNOMIAL CURVES IN FIG. 7.

Samples	$p_3$	$p_2$	$p_1$	RMSE
Saline In-Teflon Out	-1.20	2.34	1.85	0.0224
Teflon In-Saline Out	-0.20	0.71	1.84	0.0056
Gland In-Fat Out	-1.00	2.19	1.66	0.0056
Fat In-Gland Out	0.20	0.29	1.66	0.0056

The greater impact of the inner conductor radius on the sensing radius with respect to the insulator width is also illustrated in terms of electric field distribution across the probe tip and the interrogated sample in Fig. 8.

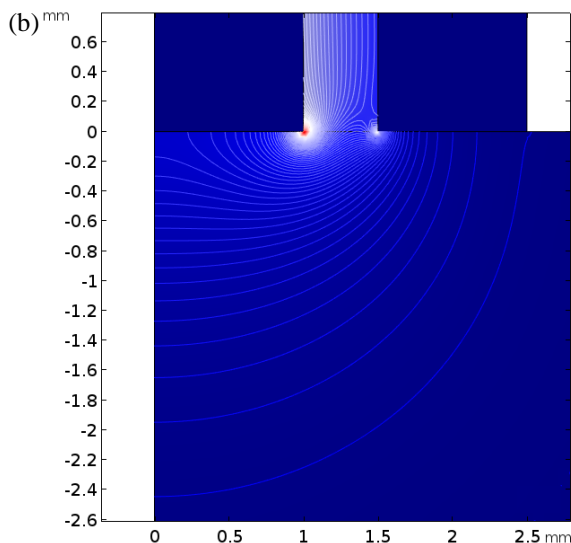
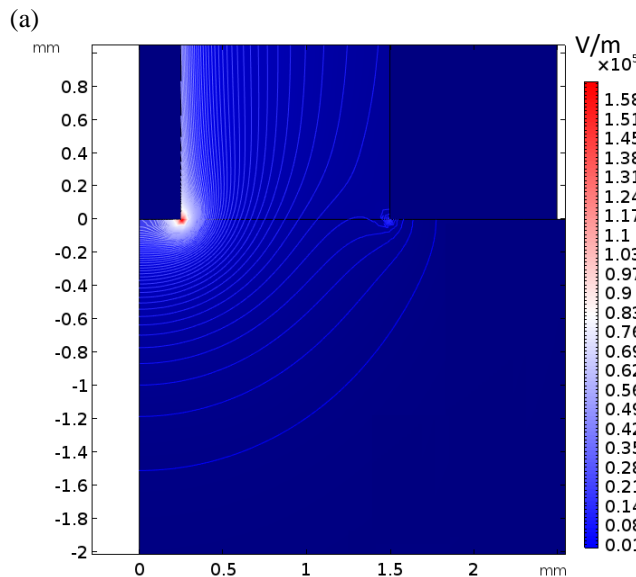


Fig. 8. Contour plot of the electric field magnitude (V/m) at 4 GHz of the simulated probes (a) CP8 and (b) CP4 in contact with Teflon surrounded by saline.

Fig. 8 depicts a simplified 2D axis-symmetric geometry, with the radial and axial distances shown in mm horizontally and vertically, respectively. The electric field isolines at 4 GHz are marked across the half cross-section of the end of the probe and the interrogated sample (Teflon surrounded by saline in this case), with the last isoline referring to the location where the electric field decay is 40 dB.

Fig. 8 a illustrates the simulated probe CP8, which has an inner conductor radius of 0.25 mm and an insulator width of 1.25 mm, while Fig. 8 b illustrates the simulated probe CP4, which has an inner conductor radius of 1 mm and an insulator width of 0.5 mm. Thus, the inner radius of the outer conductor, which is the sum of the inner conductor radius and the insulator width, is 1.5 mm for both probes. Although the two probes CP4 and CP8 have both an outer conductor inner radius of 1.5 mm, the electric field magnitude across CP4 is significantly higher than the magnitude across CP8. Also, in Fig. 8 a, the last isoline circumscribes a smaller geometrical region of the sample than the region delineated by the last isoline in Fig. 8 b, thus confirming that the inner conductor radius has higher impact than the insulator width on the sensing radius.

These results are in agreement with the findings of the study by Anderson *et al.*, for which the sensing radius does not exceed the total radius of the probe and the magnitude of the EM field is the highest in proximity of the inner conductor of the probe [18]. Furthermore, as in the study conducted by Hoshina *et al.*, by observing the electric field across all simulated samples, it was found that the magnitude of the electric field is negligible out of the hemispherical region delineated by the -40 dB isoline (the outer isoline depicted in both illustrations of Fig. 8), at which also the effect of the outer material is within the measurement uncertainty [23].

Lastly, in Fig. 9, the average sensing radii calculated across the scenarios S4 are plotted versus the radii of the inner conductor. The four probes of the subset S4 have increasing inner conductor radii and insulator widths. The data in Fig. 9 illustrates the linear relationship between the sensing radius and

the inner conductor radius across all samples. Thus, the data was interpolated with regression lines, the parameters of which are listed in Table VIII for each simulated sample. As indicated from the  $R^2$  and RMSE values, in this case, the quality of the fitting is a bit lower than in the previous cases; however, the data is still well-represented by the fitted lines. For the subset S4, since the insulator width increases while the inner conductor radius increases, a trend similar to that for the dependence of the sensing radius on the inner conductor radius was found for the dependence of the sensing radius on the insulator width.

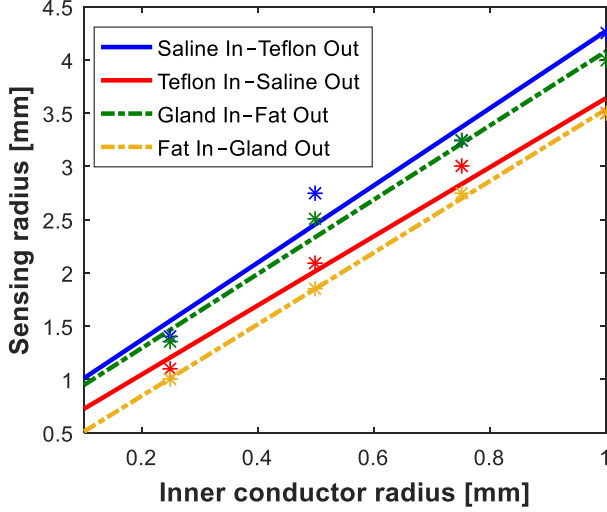


Fig. 9. Sensing radius vs inner conductor radius for the scenario S4, where both  $a$  and  $c$  are increased with  $b$ . The parameters of the regression lines fitting the sensing radius data are reported in Table VIII.

TABLE VIII  
PARAMETERS,  $R^2$  VALUE AND RMSE OF THE REGRESSION LINES IN FIG. 9.

Samples	$p_2$	$p_1$	$R^2$	RMSE
Saline In-Teflon Out	3.62	0.65	0.971	0.2470
Teflon In-Saline Out	3.24	0.40	0.980	0.1830
Gland In-Fat Out	3.48	0.60	0.987	0.1550
Fat In-Gland Out	3.36	0.18	0.999	0.0474

Before summarising and discussing the findings of the numerical results shown in this subsection, the accuracy of the linear regression model and the neural network at predicting the sensing radius is detailed in the next subsection.

### C. Sensing radius prediction

First, the ability to predict the sensing radius was examined through a linear regression model. From this modelling, a fitting line with the following equation was obtained:

$$y = -0.13 + 0.703 a + 0.907 b + 0.013 \epsilon_{r1} + 0.005 \epsilon_{r2}, \quad (5)$$

where  $y$  is the sensing radius and  $a$ ,  $b$ ,  $\epsilon_{r1}$  and  $\epsilon_{r2}$  are the input features defined in Section II.C.

Next, the neural network approach was considered. Across the ten iterations of training and testing the neural network, an average MSE of 0.0821 was calculated, ranging between the lowest value of 0.0128 and the highest value of 0.2048. The

network with the lowest MSE was selected to be used as the final optimised neural network.

By comparing the performance of the two models across the testing dataset, an average difference of 0.1 mm was obtained between the targets and the estimates from the linear regression (with the lowest difference of 0.005 mm and the highest difference of 0.193 mm), and an average difference of 0.048 mm was obtained between the targets and the estimates from the neural network (with the lowest difference of 0.004 mm and the highest difference of 0.09 mm). In addition, across the estimates from the testing stage, an average RMSE of 0.13 was obtained for the linear regression and an average RMSE of 0.05 was obtained for the network, suggesting a good match between the predicted sensing radius and the target value for both models.

The performances of the linear regression and the neural network are graphically compared in Fig. 10, where the predicted sensing radius values from the testing dataset are plotted versus the target values obtained numerically. For a better interpretation of the data, in Fig. 10, an ideal line obtained by considering a perfect match between estimates and targets ( $y = x$ ) is plotted.

Since the values predicted from the neural network are closer to the ideal line than the values predicted from the linear regression model, Fig. 10 demonstrates that the trained neural network can predict the sensing radius with a higher accuracy than the linear regression model. Specifically, while an average accuracy (obtained from the average percentage difference between estimates and targets) of 90% is obtained for the linear regression model, an average accuracy of 95% is obtained for the neural network.

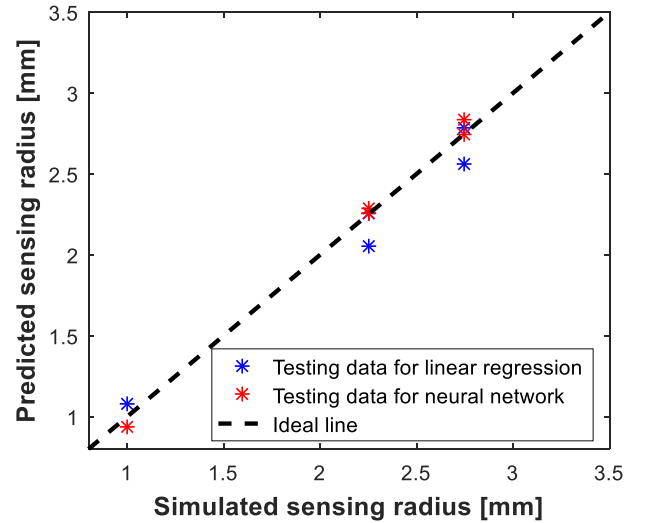


Fig. 10. Plot comparing the sensing radius data predicted by the linear regression and the neural network (estimates) with the sensing radius data obtained numerically (targets).

The performance of the two models was further tested by evaluating the sensing radius predicted from the performance and high temperature probes in a known experimental setting (as summarised in Section II.A). The performance and high temperature probes are not included among the 12 simulated probes used for the 48 simulation scenarios, which were employed to develop and test the linear regression and the neural network models. However, by comparing the dimensions

of the performance and high temperature probes summarised in Table I with those of the simulated probes listed in Table III, the performance probe features are close to those of the probe CP1, and the high temperature probe has features close to those of the probe CP2.

By providing the linear regression model with the probe dimensions and material relative permittivities, an estimate of 1.73 mm and 2.29 mm was found for the sensing radius of the performance and high temperature probes, respectively. By providing the neural network with the same inputs, estimates of 1.54 mm and 2.37 mm were found, respectively. The comparison of these predicted values with the values obtained numerically, which are 1.5 mm and 2.25 mm for the performance and high temperature probes, respectively, suggest that, while both models are possible to be implemented, a neural network can potentially outperform linear regression. In summary, these results demonstrate the potential for using neural networks, or similar algorithms, to predict the sensing radius of a coaxial probe based on knowledge of the probe dimensions and the dielectric properties of the investigated sample, with an accuracy higher than 90%.

The potential applications of the trained network are detailed in the following subsection, where all the findings of the study are summarised and discussed.

#### D. Discussion

After performing preliminary experiments that confirmed that the width of the outer conductor does not affect the sensing radius, two key findings were obtained from experiments and simulations modelling the dependence of the sensing radius on the probe dimensions.

Firstly, from the experiments conducted with the Keysight probes and the simulations performed with the probes in S1, S2 and S4, it was observed that the sensing radius increases linearly by increasing the inner radius of the outer conductor  $b$ . In fact, an increase of  $b$  results in an increase of the radial extent of the sample interrogated by the electric field, and, thus, in an increase of the sensing radius.

Furthermore, the sensing radius estimates are consistent with estimates from the literature. For instance, the sensing radius value obtained for the probe CP1 (which has dimensions similar to the dimensions of the 2.2 mm diameter probe used by Hagl *et al.*), is comparable with the sensing radius value reported by Hagl *et al.* [12]. In fact, in the numerical simulations a maximum sensing radius of 1.4 mm was obtained for the CP1 probe (illustrated by the leftmost blue star in Fig. 5, Fig. 6 and Fig. 9), which has a total radius of 1.1 mm, and in the study by Hagl *et al.*, a sensing radius of 1.25 mm was obtained for the 2.2 mm diameter probe [12]. Also, the maximum radius values obtained from the simulation subsets S1, S2 and S4 satisfy the relationship between sensing radius and probe aperture, defined by the inner radius of the outer conductor  $b$ , reported in the study by De Langhe *et al.* [19].

Secondly, from the simulated probes in S3, it was found that the radius of the inner conductor has a greater impact on the sensing radius than the insulator width. This outcome, in agreement with the study by Anderson *et al.* [18], is confirmed by Gauss's theorem, which relates the radial component of the electric field within the coaxial probe to the applied input voltage and the probe dimensions, as follows:

$$E(\rho) = \frac{\Delta V}{\ln \frac{b}{a}} \frac{1}{\rho}, \quad (6)$$

where  $E(\rho)$  is the radial component of the electric field,  $\rho$  can be any point across the radial extent of the coaxial probe between the points delineated by  $a$  and  $b$ , which are the dimensions of the probe previously defined and illustrated in Fig. 1, and  $\Delta V$  is the input voltage applied at the probe aperture between the points delineated by  $a$  and  $b$ . From (6) it is clear that, if  $b$  is fixed, the electric field at a fixed point  $\rho$  increases with  $a$ . Since the size of the sensing radius is proportional to the electric field magnitude across the probe, Gauss's theorem confirms that, at a certain location  $\rho$ , when  $b$  is fixed, the sensing radius increases with the radius of the inner conductor  $a$ .

Furthermore, the numerical study confirmed that the trends of the sensing radius with the probe dimensions are consistent across samples having different dielectric properties. However, the size of the sensing radius does depend on the complex permittivity of the interrogated sample.

In previous studies as in [12], only the information regarding the probe features were used to estimate the sensing radius. Instead, in this study, we suggest the use of a fixed sensing radius (i.e., the maximum sensing radius) for the definition of the size of the sample region to analyse histologically. Then, we recommend refining the sensing radius size based on the histological properties of the sample, since the sensing radius varies based on the tissue composition of the sample.

In particular, in the case of highly heterogeneous tissue samples, or samples with completely unknown composition, the maximum sensing radius (obtained from the sample having saline as inner material and Teflon as outer material) can be used for dielectric characterisation. In the case of tissue samples with known constituents, a sensing radius smaller than the maximum may be chosen. For example, if it is known that the sample contains only fat and gland (or similar types of tissues), the sensing radius corresponding to this specific scenario can be used.

Lastly, all of the numerical data was modelled with a regression line and also used to build a neural network. Specifically, the neural network requires as input features the radius of the inner conductor, the inner radius of the outer conductor, and the average relative permittivity of two concentric materials. The neural network is able to predict the sensing radius from a defined set of inputs with an accuracy approximately 5% higher than that of the linear regression model. With predictions always within 0.2 mm of the target sensing radius values, the neural network provides estimates that are appropriately accurate for use in experimental studies. Since the network was trained with a discrete number of geometries and a small number of interrogated materials, the neural network is likely only able to predict the sensing radius with high accuracy for breast tissue or tissues with similar dielectric properties, such as heart tissue. However, the neural network performance can be extended to any type of biological tissue by training it with an increased number of sample tissues for each probe geometry. Overall, with some additional development, such a technique could support researchers in providing a fast and easy method to estimating the sensing radius in future studies.

Future studies modelling the sensing radius for any probe and biological sample have the potential to improve the dielectric characterisation of a wide range of heterogeneous biological tissues. This characterisation enables accurate interpretation and use of dielectric data, to support the design of EM-based diagnostic and therapeutic devices.

#### IV. CONCLUSIONS

In this study, dielectric measurements and numerical simulations were conducted to investigate and model the dependence of the sensing radius of a coaxial probe on the probe dimensions.

First, both measurements and simulations were performed to determine the maximum sensing radius for each of the three Keysight probes. A maximum sensing radius of 1.4 mm, 1.5 mm, and 2.25 mm was estimated numerically for the slim form probe, performance probe, and high temperature probe, respectively. This initial outcome not only verified consistency between measurements and simulations, but also demonstrated that the sensing radius of a coaxial probe increases with increasing the inner radius of the outer conductor.

Next, in order to model the dependence of the sensing radius on the probe dimensions, a number of probes having different geometries were modelled numerically by varying, in turn, the dimensions of the inner conductor, the insulator, and the outer conductor. It was thus observed that the sensing radius: i) is not affected by the width of the outer conductor, ii) increases linearly with the inner radius of the outer conductor, and iii) is mostly affected by the radius of the inner conductor. Furthermore, although the sensing radius depends on the complex permittivity of the materials constituting the investigated sample, the trend of the sensing radius as a function of the probe dimensions is the same across different samples.

Finally, the sensing radius data calculated numerically was used to build a neural network able to predict the sensing radius of a coaxial probe within 0.2 mm, from knowledge of a subset of probe dimensions and interrogated materials.

In summary, this study modelled the dependence of the sensing radius of a coaxial probe on the probe dimensions, which supports accurate dielectric characterisation of biological tissues. In particular, this work supports accurate dielectric measurement of breast tissue, which is fundamental for the design of MW breast imaging systems.

#### REFERENCES

- [1] M. Pastorino, *Microwave imaging*. John Wiley & Sons, 2010.
- [2] A. Martellosio *et al.*, "Dielectric properties characterization from 0.5 to 50 GHz of breast cancer tissues," *IEEE Trans. Microw. Theory Tech.*, vol. 65, no. 3, pp. 998–1011, 2017, doi: 10.1109/TMTT.2016.2631162.
- [3] N. R. Datta *et al.*, "Local hyperthermia combined with radiotherapy and/or chemotherapy: Recent advances and promises for the future," *Cancer Treat. Rev.*, vol. 41, no. 9, pp. 742–753, 2015.
- [4] C. L. Brace, "Temperature-dependent dielectric properties of liver tissue measured during thermal ablation: toward an improved numerical model," in *IEEE Engineering in Medicine and Biology Society*, 2008, pp. 230–233, doi: 10.1109/IEMBS.2008.4649132.
- [5] V. Lopresto, R. Pinto, L. Farina, and M. Cavagnaro, "Treatment planning in microwave thermal ablation: clinical gaps and recent research advances," *Int. J. Hyperth.*, vol. 33, no. 1, pp. 83–100, 2017, doi: 10.1080/02656736.2016.1214883.
- [6] E. Burdette, F. Cain, and J. Seals, "In vivo probe measurement technique for determining dielectric properties at VHF through microwave frequencies," *IEEE Trans. Microw. Theory Tech.*, vol. 28, no. 4, pp. 414–427, 1980, [Online]. Available: [http://ieeexplore.ieee.org/xpls/abs\\_all.jsp?arnumber=1130087](http://ieeexplore.ieee.org/xpls/abs_all.jsp?arnumber=1130087).
- [7] S. Gabriel, R. W. Lau, and C. Gabriel, "The dielectric properties of biological tissues: II. Measurements in the frequency range 10 Hz to 20 GHz," *Phys. Med. Biol.*, vol. 41, no. 11, pp. 2251–2269, 1996, doi: 10.1088/0031-9155/41/11/002.
- [8] A. Peyman, S. Holden, and C. Gabriel, "Mobile Telecommunications and Health Research Programme: Dielectric Properties of Tissues at Microwave Frequencies," 2005. [Online]. Available: [http://www.mthr.org.uk/research\\_projects/documents/Rum3FinalReport.pdf](http://www.mthr.org.uk/research_projects/documents/Rum3FinalReport.pdf).
- [9] J. Baker-Jarvis, "NIST Technical Note 1341: Transmission / Reflection and Short-Circuit Line Permittivity Measurements, United States Department of Commerce, National Institute of Standards and Technology," 1990.
- [10] M. A. Stuchly, T. W. Athey, G. M. Samaras, and G. E. Taylor, "Measurement of Radio Frequency Permittivity of Biological Tissues with an Open-Ended Coaxial Line: Part II - Experimental Results," *IEEE Trans. Microw. Theory Tech.*, vol. 30, no. 1, pp. 87–92, 1982, doi: 10.1109/TMTT.1982.1131022.
- [11] T. W. Athey, M. A. Stuchly, and S. S. Stuchly, "Measurement of radio frequency permittivity of biological tissues with an open-ended coaxial line: Part I," *IEEE Trans. Microw. Theory Tech.*, vol. 30, no. 1, pp. 82–86, 1982.
- [12] D. Hagl, D. Popovic, S. C. Hagness, J. H. Booske, and M. Okoniewski, "Sensing volume of open-ended coaxial probes for dielectric characterization of breast tissue at microwave frequencies," *IEEE Trans. Microw. Theory Tech.*, vol. 51, no. 4, pp. 1194–1206, 2003, doi: 10.1109/TMTT.2003.809626.
- [13] D. Xu, L. Liu, and Z. Jiang, "Measurement of the dielectric properties of biological substances using an improved open-ended coaxial line resonator method," *IEEE Trans. Microw. Theory Tech.*, vol. 35, no. 12, pp. 1424–1428, 1987.
- [14] Y. Z. Wei and S. Sridhar, "Radiation-Corrected Open-Ended Coax Line Technique for Dielectric Measurements of Liquids up to 20 GHz," *IEEE Trans. Microw. Theory Tech.*, vol. 39, no. 3, pp. 526–531, 1991, doi: 10.1109/22.75296.
- [15] E. Alanen, T. Lahtinen, and J. Nuutinen, "Variational formulation of open-ended coaxial line in contact with layered biological medium," *IEEE Trans. Biomed. Eng.*, vol. 45, no. 10, pp. 1241–1248, 1998, doi: 10.1109/10.720202.
- [16] P. M. Meaney, A. P. Gregory, J. Seppälä, and T. Lahtinen, "Open-Ended Coaxial Dielectric Probe Effective Penetration Depth Determination," *IEEE Trans. Microw. Theory Tech.*, vol. 64, no. 3, pp. 915–923, 2016, doi: 10.1109/TMTT.2016.2519027.
- [17] E. Porter and M. O'Halloran, "Investigation of Histology Region in Dielectric Measurements of Heterogeneous Tissues," *IEEE Trans. Antennas Propag.*, vol. 65, no. 10, pp. 5541–5552, 2017.
- [18] L. S. Anderson, G. B. Gajda, and S. S. Stuchly, "Analysis of an Open-Ended Coaxial Line Sensor in Layered Dielectrics," *IEEE Trans. Instrum. Meas.*, vol. IM-35, no. 1, pp. 13–18, 1986, doi: 10.1109/TIM.1986.6499049.
- [19] P. De Langhe, L. Martens, and D. De Zutter, "Design Rules for an Experimental Setup Using an Open-Ended Coaxial Probe Based on Theoretical Modelling," *IEEE Trans. Instrum. Meas.*, vol. 43, no. 6, pp. 810–817, 1994, doi: 10.1109/19.368062.
- [20] K. Folgerø and T. Tjomsland, "Permittivity measurement of thin liquid layers using open-ended coaxial probes," *Meas. Sci. Technol.*, vol. 7, no. 8, pp. 1164–1173, 1996, doi: 10.1088/0957-0233/7/8/012.
- [21] S. Huclova, D. Baumann, M. Talary, and J. Fröhlich, "Sensitivity and specificity analysis of fringing-field dielectric spectroscopy applied to a multi-layer system modelling the human skin," *Phys. Med. Biol.*, vol. 56, no. 24, pp. 7777–7793, 2011, doi: 10.1088/0031-9155/56/24/007.
- [22] P. M. Meaney, A. Gregory, N. Epstein, and K. D. Paulsen, "Microwave open-ended coaxial dielectric probe: interpretation of the sensing volume re-visited," *BMC Med. Phys.*, vol. 14, no. 1, pp. 1–11, 2014, doi:

10.1186/1756-6649-14-3.

- [23] S. Hoshina, Y. Kanai, and M. Miyakawa, "A numerical study on the measurement region of an open-ended coaxial probe used for complex permittivity measurement," *IEEE Trans. Magn.*, vol. 37, no. 5, pp. 3311–3314, 2001, doi: 10.1109/20.952602.
- [24] A. La Gioia, M. O'Halloran, and E. Porter, "Modelling the Sensing Radius of a Coaxial Probe for Dielectric Characterisation of Biological Tissues," *IEEE Access*, vol. 6, pp. 46516–46526, 2018, doi: 10.1109/ACCESS.2018.2866703.
- [25] M. Lazebnik *et al.*, "A large-scale study of the ultrawideband microwave dielectric properties of normal, benign and malignant breast tissues obtained from cancer surgeries," *Phys. Med. Biol.*, vol. 52, no. 20, pp. 6093–6115, 2007, doi: 10.1088/0031-9155/52/20/002.
- [26] M. Lazebnik *et al.*, "A large-scale study of the ultrawideband microwave dielectric properties of normal breast tissue obtained from reduction surgeries," *Phys. Med. Biol.*, vol. 52, no. 10, pp. 2637–2656, 2007, doi: 10.1088/0031-9155/52/10/001.
- [27] A. La Gioia, M. O'Halloran, A. Elahi, and E. Porter, "Investigation of Histology Radius for Dielectric Characterisation of Heterogeneous Materials," *IEEE Trans. Dielectr. Insul.*, vol. 25, no. 3, pp. 1065–1080, 2018.
- [28] L. Abdilla, C. Sammut, and L. Mangion, "Dielectric properties of muscle and liver from 500 MHz–40 GHz," *Electromagn. Biol. Med.*, vol. 32, no. 2, pp. 244–252, 2013, doi: 10.3109/15368378.2013.776436.
- [29] R. J. Halter *et al.*, "The correlation of in vivo and ex vivo tissue dielectric properties to validate electromagnetic breast imaging: initial clinical experience," *Physiol. Meas.*, vol. 30, no. 6, pp. S121–S136, 2009, doi: 10.1088/0967-3334/30/6/S08.
- [30] A. Peyman *et al.*, "Variation in dielectric properties due to pathological changes in human liver," *Bioelectromagnetics*, vol. 36, no. 8, pp. 603–612, 2015, doi: 10.1002/bem.21939.
- [31] Keysight, "N1501A Dielectric Probe Kit 10 MHz to 50 GHz: Technical Overview. Available at: <http://www.keysight.com/en/pd-2492144-pn-N1501A/dielectric-probe-kit>. [Accessed 30 October 2017].," 2015. [Online]. Available: <http://www.keysight.com/en/pd-2492144-pn-N1501A/dielectric-probe-kit>.
- [32] T. Sugitani *et al.*, "Complex permittivities of breast tumor tissues obtained from cancer surgeries," *Appl. Phys. Lett.*, vol. 104, no. 25, p. (253702)1–5, 2014, doi: 10.1063/1.4885087.
- [33] C. Gabriel and A. Peyman, "Dielectric measurement: error analysis and assessment of uncertainty," *Phys. Med. Biol.*, vol. 51, no. 23, pp. 6033–6046, 2006, doi: 10.1088/0031-9155/51/23/006.
- [34] S. Salahuddin, E. Porter, F. Krewer, and M. O'Halloran, "Optimised analytical models of the dielectric properties of biological tissue," *Med. Eng. Phys.*, vol. 43, pp. 103–111, 2017, doi: 10.1016/j.medengphy.2017.01.017.
- [35] D. Berube, F. M. Ghannouchi, and P. Savard, "A Comparative Study of Four Open-Ended Coaxial Probe Models for Permittivity Measurements of Lossy Dielectric/Biological Materials at Microwave Frequencies," *IEEE Trans. Microw. Theory Tech.*, vol. 44, no. 10, pp. 1928–1934, 1996, doi: 10.1080/10420150214608.
- [36] P. Hasgall *et al.*, "IT'IS Database for thermal and electromagnetic parameters of biological tissues," *Version 4.0*, 2018. [www.itis.ethz.ch/database](http://www.itis.ethz.ch/database).



**Ms. Alessandra La Gioia** is a Ph.D. student in the Translational Medical Device Laboratory, funded by European Research Council and led by Dr. Martin O'Halloran, at National University of Ireland, Galway (NUIG). She completed her Bachelor's and Master's degrees in Biomedical Engineering at the University of Bologna (Italy) with first-class honours. Currently, she is investigating techniques for the

analysis of the dielectric properties of biological tissues, as a platform for low-cost medical device design.



**Dr. Adam Santorelli** (S'11 – M'18) is currently a postdoctoral researcher in the Translational Medical Device Lab. He completed his B. Eng in Electrical Engineering in 2010, his M. Eng in Electromagnetics in 2012, and his Ph.D. in 2017, at McGill University in Montreal, Canada. Adam's research interests are focused on biomedical applications with the primary goal of increasing the accessibility to technology in order to improve diagnosis, including the optimization and miniaturization of off-the-shelf components to design and fabricate custom built low-cost microwave systems. He received the 2nd Place Best Student Paper Award at the 2014 IEEE Sensors Application Symposium.



**Dr. Martin O'Halloran** received a B.Eng. (Hons.) and Ph.D. in Engineering from the National University of Ireland Galway (NUIG) in 2004 and 2009, respectively. He also holds an MSc. in Clinical Research (2014), also from NUIG. Dr. O'Halloran is the Director of the Translational Medical Device Lab at NUIG, and is a co-Director of the BioInnovate Programme (an affiliate of Stanford's BioDesign Programme). He has over 25 national and international awards, including Engineers Ireland Engineer of the Year 2014, Science Foundation Ireland's EC Researcher of the Year 2016, and the Irish Research Council Researcher of the Year 2018. Dr. O'Halloran's research is funded by Science Foundation Ireland, the Irish Research Council and the European Research Council. His research is focused on patient-centred medical device design and development.



**Dr. Emily Porter** received her B.Eng., M.Eng., and Ph.D. degrees in electrical engineering from McGill University, Montreal, Canada, in 2009, 2010, and 2015 respectively. Dr. Porter was a recipient of the 2013 IEEE Antennas and Propagation Society Doctoral Research Award for her work on breast health monitoring using a time-domain microwave system. Dr. Porter worked as an EU Marie-Curie Fellow with the Translational Medical Device Laboratory at the National University of Ireland Galway, where she conducted research on electromagnetic medical technologies. She is now an Assistant Professor at The University of Texas at Austin. Her current research interests include the measurement of dielectric properties of biological tissues and the development novel technologies for therapeutic and diagnostic applications of electromagnetic waves.